Intrinsic Second-Order Anomalous Hall Effect and Its Application in Compensated Antiferromagnets

Huiying Liu,[1] Jianzhou Zhao,[1,2,*] Yue-Xin Huang,[1] Weikang Wu,[1,3] Xian-Lei Sheng,[4] Cong Xiao,[5,6,7,†] and Shengyuan A. Yang[1]

[1]*Research Laboratory for Quantum Materials, Singapore University of Technology and Design, Singapore 487372, Singapore*
[2]*Co-Innovation Center for New Energetic Materials, Southwest University of Science and Technology, Mianyang 621010, China*
[3]*Division of Physics and Applied Physics, School of Physical and Mathematical Sciences, Nanyang Technological University, Singapore 637371, Singapore*
[4]*School of Physics, Beihang University, Beijing 100191, China*
[5]*Department of Physics, The University of Hong Kong, Hong Kong, China*
[6]*HKU-UCAS Joint Institute of Theoretical and Computational Physics, Hong Kong, China*
[7]*Department of Physics, The University of Texas at Austin, Austin, Texas 78712, USA*

(Received 25 July 2021; accepted 23 November 2021; published 27 December 2021)

Response properties that are purely intrinsic to physical systems are of paramount importance in physics research, as they probe fundamental properties of band structures and allow quantitative calculation and comparison with experiment. For anomalous Hall transport in magnets, an intrinsic effect can appear at the second order to the applied electric field. We show that this intrinsic second-order anomalous Hall effect is associated with an intrinsic band geometric property—the dipole moment of Berry-connection polarizability (BCP) in momentum space. The effect has scaling relation and symmetry constraints that are distinct from the previously studied extrinsic contributions. Particularly, in antiferromagnets with $\mathcal{PT}$ symmetry, the intrinsic effect dominates. Combined with first-principles calculations, we demonstrate the first quantitative evaluation of the effect in the antiferromagnet Mn_2Au. We show that the BCP dipole and the resulting intrinsic second-order conductivity are pronounced around band near degeneracies. Importantly, the intrinsic response exhibits sensitive dependence on the Néel vector orientation with a 2π periodicity, which offers a new route for electric detection of the magnetic order in $\mathcal{PT}$-invariant antiferromagnets.

DOI: 10.1103/PhysRevLett.127.277202

The anomalous Hall effect (AHE) is a fundamental transport phenomenon in which a transverse charge current is generated in response to a longitudinal electric field without external magnetic fields. The underlying mechanisms are classified into intrinsic and extrinsic ones, depending on whether or not the mechanism is related to carrier scattering [1–3]. In the study of linear AHE, a great success in the past twenty years is the recognition of the importance of the intrinsic contribution and its connection to a band geometric quantity—the Berry curvature [4,5]. Recently, the research on AHE has been extended to the nonlinear regime. Sodemann and Fu [6] proposed an *extrinsic* second-order AHE, which involves the dipole of Berry curvature and is linear in the relaxation time. In fact, before Ref. [6], an *intrinsic* second-order AHE has been predicted by Gao *et al.* [7], but received less attention. Particularly, the physical content of this intrinsic effect has not been fully understood, and furthermore, it has not been explored in any concrete material yet.

Meanwhile, in the field of spintronics, a recent focus is to utilize compensated antiferromagnets for device applications, owing to their advantages like robustness to external magnetic perturbations, absence of stray fields, and ultrafast dynamics [8–10]. Especially, the class of $\mathcal{PT}$-symmetric antiferromagnets have been attracting great interest, as they permit a fieldlike spin-orbit torque to control the Néel vectors [11], which has been successfully demonstrated in materials like CuMnAs [12–15] and Mn_2Au [16–18]. However, an outstanding challenge is how to read out the information, i.e., to detect the Néel vector orientation in these systems. Conventional magnetic measurements fail due to the absence of net magnetization [9]; optical microscopy works [13,19,20] but is difficult to incorporate for compact devices; and the approach based on anisotropic magnetoresistance (AMR) effect [9,12] suffers from the limited reading speed and cannot distinguish a 180° reversal [21]. Very recently, Shao *et al.* [22] suggested that for antiferromagnets with broken $\mathcal{PT}$ such as CuMnSb, the extrinsic second-order AHE could be used to detect the Néel vector. Unfortunately, this cannot apply for $\mathcal{PT}$-symmetric antiferromagnets, since the Berry curvature and hence the effect are suppressed by the $\mathcal{PT}$ symmetry.

In this work, we address the above challenge by showing that the intrinsic second-order AHE offers a powerful tool

for electrically detecting Néel vectors in $\mathcal{PT}$-symmetric antiferromagnets. We show that the intrinsic effect has a quantum origin connected to the dipole moment of the Berry-connection polarizability (BCP) tensor in momentum space. We clarify the symmetry characters of the effect, and point out its dominant role in $\mathcal{PT}$-symmetric antiferromagnets, where all Berry curvature related first and second order Hall responses are forbidden. Combining the theory with first-principles calculations, we perform the first quantitative evaluation of the intrinsic second-order AHE in the paradigmatic $\mathcal{PT}$-symmetric antiferromagnet Mn_2Au. The result is found to be sizable and sensitive to the Néel vector with a 2π periodicity, indicating a precise way to map out the Néel vector orientation.

Intrinsic second-order AHE and BCP dipole.—The intrinsic contribution to the second-order AHE is most easily derived within the extended semiclassical theory, which includes field corrections to the band quantities [7,23–26]. In particular, the Berry connection acquires a gauge-invariant correction $\boldsymbol{\mathcal{A}}^E$ by the applied electric field $\boldsymbol{E}$, with

$$\mathcal{A}_a^E(\boldsymbol{k}) = G_{ab}(\boldsymbol{k})E_b, \tag{1}$$

where the subscripts $a, b, \cdots$ denote Cartesian coordinates (Einstein summation convention assumed), and G_{ab} is the BCP tensor [7,27]. For a band with index n, BCP can be expressed as (we set $e = \hbar = 1$) [28]

$$G_{ab}^n(\boldsymbol{k}) = 2\mathrm{Re}\sum_{m\neq n}\frac{\mathcal{A}_a^{nm}(\boldsymbol{k})\mathcal{A}_b^{mn}(\boldsymbol{k})}{\varepsilon_n(\boldsymbol{k}) - \varepsilon_m(\boldsymbol{k})}, \tag{2}$$

where $\mathcal{A}_a^{nm} = \langle u_n | i\partial_a | u_m\rangle$ is the usual interband Berry connection, $|u_n\rangle$ is the unperturbed eigenstate, $\partial_a \equiv \partial_{k_a}$, and ε_n is the unperturbed band energy.

This generates a field-induced Berry curvature $\boldsymbol{\Omega}^E = \nabla_{\boldsymbol{k}} \times \boldsymbol{\mathcal{A}}^E$, which acts like magnetic field in momentum space and leads to an anomalous velocity term $\sim \boldsymbol{E} \times \boldsymbol{\Omega}^E$ for electrons. This velocity is transverse to the applied $\boldsymbol{E}$ field, of E^2 order, and independent of scattering, so it results in the intrinsic second-order AHE current $\boldsymbol{j}^{\mathrm{int}}$ [7]. By writing $j_a^{\mathrm{int}} = \chi_{abc}^{\mathrm{int}} E_b E_c$, we have

$$\chi_{abc}^{\mathrm{int}} = \int_{\mathrm{BZ}} \frac{d\boldsymbol{k}}{(2\pi)^d}\Lambda_{abc}(\boldsymbol{k}), \tag{3}$$

with

$$\Lambda_{abc}(\boldsymbol{k}) = -\sum_n (\partial_a G_{bc}^n - \partial_b G_{ac}^n) f_0, \tag{4}$$

where BZ stands for the Brillouin zone, d is the dimensionality of the system, and f_0 is the equilibrium Fermi-Dirac distribution. One observes that the effect is indeed intrinsic, free of scattering effects, and involving only intrinsic band geometric quantity, and more precisely, the integrand Λ represents a (antisymmetrized) combination of the momentum-space dipole moment of BCP over the occupied states. Via an integration by parts, it is also clear that the transport is a Fermi surface property, as it should be.

As its most important character, the intrinsic conductivity tensor χ^{int} here is completely determined by the band structure, hence can be precisely evaluated from first-principles calculations. This is in contrast to the extrinsic second-order response χ^{BCD} from Berry-curvature dipole in Ref. [6], which is linear in the scattering time τ. This difference also manifests in their different symmetry properties under time reversal operation: χ^{int} is $\mathcal{T}$ odd, whereas χ^{BCD} is $\mathcal{T}$ even. Thus, the intrinsic contribution requires broken $\mathcal{T}$, as in magnets, but the extrinsic one does not. Nevertheless, as mentioned, in $\mathcal{PT}$-symmetric antiferromagnets, χ^{BCD} is forbidden, but χ^{int} is allowed. And in cases where both contributions coexist, they can be distinguished in experiment by their different scaling with τ.

Symmetry property.—We have seen that the intrinsic second-order conductivity χ^{int} is a $\mathcal{T}$-odd rank-3 tensor. From Eq. (4), it is clear that $\chi_{abc}^{\mathrm{int}}$ is antisymmetric in its first two indices, which ensures that $j_a^{\mathrm{int}} E_a = 0$, i.e., $\boldsymbol{j}^{\mathrm{int}}$ is indeed a Hall current.

For most transport experiments, the setup has a planar geometry, with the applied $\boldsymbol{E}$ field and the generated current both within the plane (denoted as the xy plane). Then the effect is specified by only two tensor elements, $\chi_{xyy}^{\mathrm{int}}$ and $\chi_{yxx}^{\mathrm{int}}$. For $\boldsymbol{E}$ field making an angle θ from the x direction (usually taken to be certain crystal direction), i.e., $\boldsymbol{E} = E(\cos\theta, \sin\theta)$, the measured in-plane second-order intrinsic anomalous Hall current can be expressed as [29]

$$j_{\mathrm{AH}}^{(2)} = \chi_{\mathrm{AH}} E^2, \tag{5}$$

with

$$\chi_{\mathrm{AH}} = \chi_{yxx}^{\mathrm{int}}\cos\theta - \chi_{xyy}^{\mathrm{int}}\sin\theta. \tag{6}$$

The form of χ^{int} is also constrained by the point group symmetry of the system. Given its antisymmetry in the first two indices, to analyze its symmetry, it is convenient to transform it to an equivalent rank-2 pseudotensor

$$\mathcal{X}_{cd} = \epsilon_{abc}\chi_{abd}^{\mathrm{int}}/2, \tag{7}$$

where ϵ_{abc} is the Levi-Civita symbol. Then, the constraints from point group symmetries on $\mathcal{X}$ can be derived from

$$\mathcal{X} = \eta_T \det(O) O \mathcal{X} O^{-1}, \tag{8}$$

where O is a point group operation, and the factor $\eta_T = \pm$ is again associated with the character of χ^{int} being $\mathcal{T}$ odd:

TABLE I. Constraints on the in-plane tensor elements of $\chi^{\rm int}$ and $\chi^{\rm BCD}$ from point group symmetries. "✓" ("×") means the element is symmetry allowed (forbidden). Here, $C^z_{3,4,6}\mathcal{T}$ are not included, as they prohibit all of the listed elements.

	$\mathcal{P}$	C^z_n	C^x_n	σ_z	σ_x	$S^z_{4,6}$	S^x_4	S^x_6	$\mathcal{T}$	$\mathcal{PT}$	$C^z_2\mathcal{T}$	$C^x_2\mathcal{T}$	$C^x_{3,6}\mathcal{T}$	$C^x_4\mathcal{T}$	$\sigma_z\mathcal{T}$	$\sigma_x\mathcal{T}$	$S^z_{4,6}\mathcal{T}$	$S^x_4\mathcal{T}$	$S^x_6\mathcal{T}$
$\chi^{\rm int}_{yxx}$	×	×	×	✓	✓	×	×	×	×	✓	✓	✓	×	×	×	×	×	×	×
$\chi^{\rm int}_{xyy}$	×	×	✓	✓	×	×	✓	×	×	✓	✓	×	×	✓	×	✓	×	✓	✓
$\chi^{\rm BCD}_{yxx}$	Same as $\chi^{\rm int}$ above								✓	×	×	×	×	×	✓	✓	×	×	×
$\chi^{\rm BCD}_{xyy}$									✓	×	×	✓	✓	✓	✓	×	×	✓	×

$\eta_T = -1$ for primed operations, i.e., the magnetic symmetry operations of the form $R\mathcal{T}$ with R a spatial operation; and $\eta_T = +1$ for nonprimed operations. Here, the presence absence of $\eta_T = -1$ for primed operations is the key distinction between the intrinsic $\chi^{\rm int}$ and the extrinsic $\chi^{\rm BCD}$ contributions. In Table I, we list and compare the constraints of common point group operations on the in-plane χ tensor elements. One finds that several primed operations, such as $\mathcal{PT}$, $C^z_2\mathcal{T}$, and $S^x_6\mathcal{T}$, can completely suppress $\chi^{\rm BCD}$ but allow nonvanishing $\chi^{\rm int}$.

A model study.—To better understand the features of BCP dipole and the intrinsic second-order AHE, we first apply our theory to a four-band Dirac model. Imposing the $\mathcal{PT}$ symmetry represented by $\mathcal{PT} = -i\sigma_y K$ with K being the complex conjugation, the most general four-band $\mathcal{PT}$-symmetric Dirac model has the form [39]

$$\mathcal{H}(\boldsymbol{k}) = d_0(\boldsymbol{k}) + d_1(\boldsymbol{k})\tau_x + d_2(\boldsymbol{k})\tau_z + d_3(\boldsymbol{k})\tau_y\sigma_x + d_4(\boldsymbol{k})\tau_y\sigma_y + d_5(\boldsymbol{k})\tau_y\sigma_z, \tag{9}$$

where the τ's and σ's are two sets of Pauli matrices, and the d_i's are real functions of $\boldsymbol{k}$. To be specific, let us consider the following Dirac model in two dimensions:

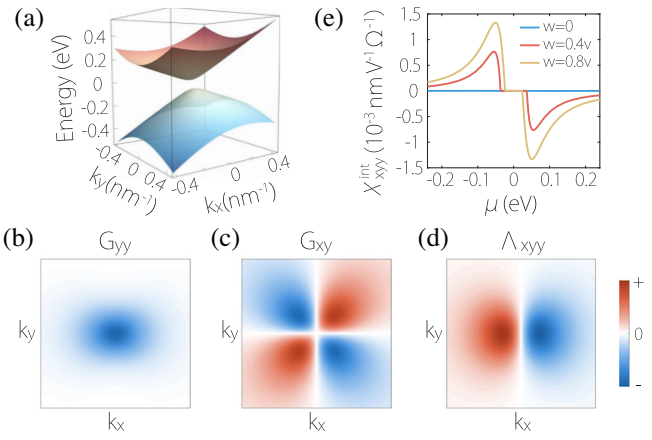

FIG. 1. (a) Band structure of the 2D Dirac model. (b)–(d) Distribution of BCP elements (b) G_{yy}, (c) G_{xy}, and (d) BCP dipole Λ_{xyy} in the momentum space for the valence bands of the model. (e) Calculated intrinsic second-order anomalous Hall conductivity $\chi^{\rm int}_{xyy}$ versus the Fermi energy μ. In the calculation, we take $v_x = v_y = 1 \times 10^6$ m/s, $w = 0.4v_x$, and $\Delta = 40$ meV.

$$\mathcal{H} = wk_x + v_xk_x\tau_x + v_yk_y\tau_y\sigma_x + \Delta\tau_z, \tag{10}$$

where w, v_i's, and Δ are real parameters. The energy spectrum is given by $\varepsilon_\pm(\boldsymbol{k}) = wk_x \pm \sqrt{v_x^2k_x^2 + v_y^2k_y^2 + \Delta^2}$, where each band has a twofold degeneracy due to the $\mathcal{PT}$ symmetry [see Fig. 1(a)]. The last term in Eq. (10) is a mass term; when $\Delta = 0$, the bands cross at a fourfold Dirac point at zero energy. The first term wk_x represents a tilt of the Dirac-cone dispersion.

For this model, the nonvanishing contribution in Eq. (6) comes from $\chi^{\rm int}_{xyy}$. The relevant BCP elements G_{yy} and G_{xy} as well as the BCP dipole Λ_{xyy} for the valence bands are plotted in Figs. 1(b)–1(d). One observes that G_{yy} and G_{xy}, respectively show a monopole and a quadrupole pattern in momentum space, and the resulting Λ_{xyy} exhibits a dipole pattern along k_x. All these quantities are concentrated around the small-gap region. In Fig. 1(e), we plot $\chi^{\rm int}_{xyy}$ as a function of the Fermi energy μ. One can see that the response is pronounced when μ is close to the small gap region. It is also noted that the tilt term plays an important role, as it lowers the symmetry to allow nonvanishing BCP dipole and $\chi^{\rm int}$.

The model study illustrates a general feature, namely, like Berry curvature, the BCP and its dipole are concentrated around small-gap regions in the band structure, and the resulting nonlinear response is therefore enhanced when the Fermi level is near such regions.

In the Supplemental Material [29], we present a detailed study of several other Dirac models, including the type-II case where the tilt term dominates the dispersion. The obtained results are very similar and confirm the general feature discussed above. These results could be helpful for understanding the effect in $\mathcal{PT}$-symmetric antiferromagnets with Dirac points or nodal lines around the Fermi level [39–41].

Application to Mn_2Au.—As its unique advantage, the intrinsic second-order AHE only depends on the band structure, thus it can be evaluated in first-principles calculations to yield quantitative predictions for concrete materials. Here, we consider Mn_2Au, which is a paradigmatic example of $\mathcal{PT}$-symmetric antiferromagnets and is under active research in recent years [16–18,42–44].

The lattice structure of Mn_2Au is shown in Fig. 2, which is tetragonal and belongs to the space group $I4/mmm$

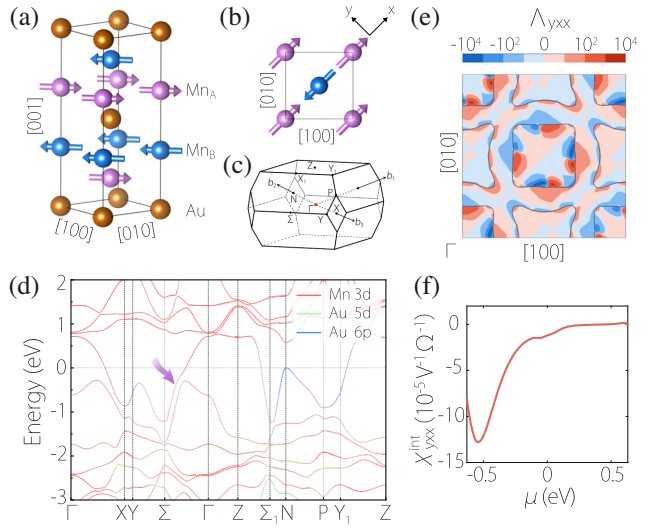

FIG. 2. (a) Crystal structure of Mn_2Au. Mn atoms with opposite magnetic moments are marked with two different colors. Black lines indicate the conventional unit cell. (b) In the ground state, the Néel vector is along the [110] direction, which is labeled as the x axis here. (c) The Brillouin zone. (d) Calculated band structure of antiferromagnetic Mn_2Au. The arrow indicates the small gap region that contributes to the peak in (f). (e) Distribution of Λ_{yxx} in the $k_z = 0$ plane of the BZ, in the unit of $\text{Å}^3 \cdot \text{V}^{-1}$. Black lines depict the Fermi surface. (f) Calculated χ^{int}_{yxx} versus the Fermi energy μ.

(No. 139). Experiment shows that Mn_2Au is a good metal, with compensated collinear antiferromagnetism and a high Néel temperature > 1000 K [43]. The ground state magnetic configuration is illustrated in Fig. 2. The magnetic moments are coupled ferromagnetically within each Mn sheet normal to c, whereas two neighboring sheets are antiferromagnetically coupled. The Néel vector $\boldsymbol{N}$ shows a strong in-plane anisotropy and it prefers the $\langle 110 \rangle$ direction. Our first-principles calculations based on the density functional theory (DFT) confirm these features (calculation details are presented in the Supplemental Material [29]).

The magnetic configuration of Mn_2Au belongs to the $Fm'mm$ magnetic space group. Importantly, it preserves $\mathcal{PT}$, which suppresses the extrinsic contribution χ^{BCD} to the second-order response. In addition, for $\boldsymbol{N}$ along the [110] direction which is chosen to be the x direction here [see Fig. 2(b)], the preserved symmetries M_x and $M_y\mathcal{T}$ dictate that χ^{int}_{xyy} vanishes, and only χ^{int}_{yxx} is needed for describing the in-plane intrinsic second-order Hall transport.

Figure 2(d) shows our calculated band structure for Mn_2Au along with the projection onto atomic orbitals. One observes that the low-energy states around the Fermi level are mostly contributed by the Mn-3d orbitals and Au-5p orbitals. In Fig. 2(e), we plot the BCP dipole Λ_{yxx} for the $k_z = 0$ plane in the BZ. It is an even function with respect to M_x. Again, we see that pronounced contributions are from the small-gap region close to the Fermi level, as indicated in Fig. 2(d). Nevertheless, the small-gap region here has a complicated extended shape, which cannot be described by any simple model, so we have to proceed with numerical calculations. χ^{int}_{yxx} is obtained as the integral of the BCP dipole over the whole BZ. In Fig. 2(f), we further show χ^{int}_{yxx} as a function of the Fermi energy. Without doping, χ^{int}_{yxx} has a value about $-1.2 \times 10^{-5}\ \text{V}^{-1}\,\Omega^{-1}$. Taking the room-temperature resistivity $\rho \sim 22\ \mu\Omega \cdot \text{cm}$ from experiment [44], we estimate that for a sample of lateral size $\sim 100\ \mu$m, under a moderate longitudinal current density of $5 \times 10^6\ \text{A/cm}^2$, the induced intrinsic nonlinear Hall voltage is $\sim 0.03\ \mu$V, which can be detected in experiment. Figure 2(f) also shows that the effect would be greatly enhanced by an order of magnitude when the Fermi energy is shifted towards -0.5 eV, due to the band near degeneracy located at that energy [see Fig. 2(d)].

Most importantly, we show that the intrinsic second-order AHE sensitively depends on the Néel vector direction, thereby it serves as a powerful tool for detecting $\boldsymbol{N}$. For example, we fix the driving field and the measurement directions to be along x and y, respectively. Then the response is specified by χ^{int}_{yxx}. Figure 3 shows the variation of χ^{int}_{yxx} when the Néel vector rotates in the xy plane (here $\boldsymbol{N}$ is defined to be along the moments of the purple-colored sublattice). This variation comes about because the band structure and hence the BCP dipole depend on the direction of the Néel vector [29]. Importantly, χ^{int}_{yxx} exhibits a 2π periodicity, meaning that the measurement is capable of fully mapping out the Néel vector orientation. This is in contrast to measurement based on linear AMR [12,16], which has a π periodicity and cannot distinguish a 180° reversal. Here, the 180° reversal would flip the sign of the signal, as $\chi^{\text{int}}(\alpha) = -\chi^{\text{int}}(\alpha + \pi)$ where α is the polar angle of $\boldsymbol{N}$. In Fig. 3, we also include the curve for χ^{int}_{xyy}. In fact, due to the C_4^z symmetry, χ^{int}_{xyy} is not independent, but related to χ^{int}_{yxx} via $\chi^{\text{int}}_{xyy}(\alpha) = -\chi^{\text{int}}_{yxx}(\alpha - \pi/2)$. Thus, the in-plane

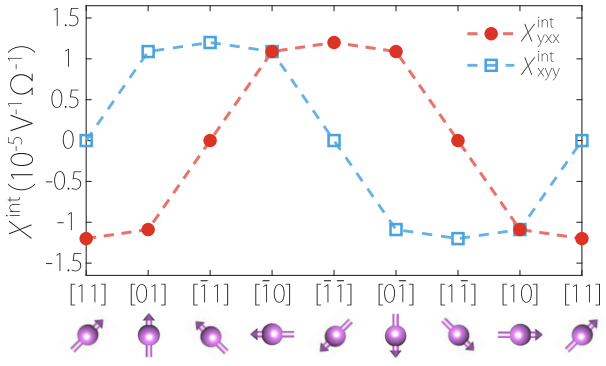

FIG. 3. (a) Calculated intrinsic second-order conductivity χ^{int}_{yxx} and χ^{int}_{xyy} of Mn_2Au when the Néel vector (denoted by the moment orientation of Mn_A) rotates in the xy plane.

intrinsic second-order AHE here can be completely specified by a single tensor element.

Discussion.—We have shown that the intrinsic second-order AHE offers a new route for probing the BCP dipole, which is an intriguing band geometric quantity, and for detecting Néel vectors, which is a challenge in antiferromagnetic spintronics. We demonstrate the first-principles evaluation of the effect for a concrete material. The study can be naturally extended to other materials such as MgMnGe, $MnPd_2$, and CuMnAs, also including magnets without $\mathcal{PT}$, as long as the effect is symmetry allowed.

We focus on the intrinsic effect in this work. Similar to the linear AHE, there are other extrinsic contributions in the second-order response, but they typically exhibit different behaviors. As mentioned, the Berry curvature dipole induced one (and also the conventional Drude contribution) can be distinguished from the intrinsic one by their different scalings with τ [45,46]. It has also been shown that the extrinsic contributions in the zeroth-order of scattering time from the so-called coordinate shift and skew scattering mechanisms are suppressed by the $\mathcal{PT}$ symmetry [47].

In practice, the effect can be measured with the standard Hall bar setup as in Refs. [45,46,48]. For $\mathcal{PT}$-symmetric antiferromagnets, it has been experimentally demonstrated that the Néel vector can be rotated by current pulse via the fieldlike spin-orbit torques [12–18]. Combined with the detection scheme by the intrinsic second-order AHE proposed here, it is possible to achieve a full-electric "write-in" and "read-off" device based on antiferromagnetic platforms, which is a central goal of the field.

The authors thank D. L. Deng for helpful discussions. This work is supported by the Singapore MOE AcRF Tier 2 (Grant No. MOE2019-T2-1-001), the National Natural Science Foundation of China (No. 11604273), the UGC/RGC of Hong Kong SAR (AoE/P-701/20), and the NSFC (Grant No. 12174018).

Note added.—Recently, a complementary and independent study [49] appeared, with similar theory and calculation done for a different material.

*jzzhao@swust.edu.cn
†congxiao@hku.hk

[1] N. A. Sinitsyn, J. Phys. Condens. Matter **20**, 023201 (2008).
[2] N. Nagaosa, J. Sinova, S. Onoda, A. H. MacDonald, and N. P. Ong, Rev. Mod. Phys. **82**, 1539 (2010).
[3] D. Xiao, M.-C. Chang, and Q. Niu, Rev. Mod. Phys. **82**, 1959 (2010).
[4] T. Jungwirth, Q. Niu, and A. H. MacDonald, Phys. Rev. Lett. **88**, 207208 (2002).
[5] M. Onoda and N. Nagaosa, J. Phys. Soc. Jpn. **71**, 19 (2002).
[6] I. Sodemann and L. Fu, Phys. Rev. Lett. **115**, 216806 (2015).
[7] Y. Gao, S. A. Yang, and Q. Niu, Phys. Rev. Lett. **112**, 166601 (2014).
[8] T. Jungwirth, X. Marti, P. Wadley, and J. Wunderlich, Nat. Nanotechnol. **11**, 231 (2016).
[9] V. Baltz, A. Manchon, M. Tsoi, T. Moriyama, T. Ono, and Y. Tserkovnyak, Rev. Mod. Phys. **90**, 015005 (2018).
[10] L. Šmejkal, Y. Mokrousov, B. Yan, and A. H. MacDonald, Nat. Phys. **14**, 242 (2018).
[11] J. Železny, H. Gao, K. Výborný, J. Zemen, J. Mašek, A. Manchon, J. Wunderlich, J. Sinova, and T. Jungwirth, Phys. Rev. Lett. **113**, 157201 (2014).
[12] P. Wadley *et al.*, Science **351**, 587 (2016).
[13] M. J. Grzybowski, P. Wadley, K. W. Edmonds, R. Beardsley, V. Hills, R. P. Campion, B. L. Gallagher, J. S. Chauhan, V. Novak, T. Jungwirth, F. Maccherozzi, and S. S. Dhesi, Phys. Rev. Lett. **118**, 057701 (2017).
[14] P. Wadley, S. Reimers, M. J. Grzybowski, C. Andrews, M. Wang, J. S. Chauhan, B. L. Gallagher, R. P. Campion, K. W. Edmonds, S. S. Dhesi, F. Maccherozzi, V. Novak, J. Wunderlich, and T. Jungwirth, Nat. Nanotechnol. **13**, 362 (2018).
[15] J. Godinho, H. Reichlová, D. Kriegner, V. Novák, K. Olejník, Z. Kašpar, Z. Šobáň, P. Wadley, R. P. Campion, R. M. Otxoa, P. E. Roy, J. Železný, T. Jungwirth, and J. Wunderlich, Nat. Commun. **9**, 4686 (2018).
[16] S. Y. Bodnar, L. Šmejkal, I. Turek, T. Jungwirth, O. Gomonay, J. Sinova, A. A. Sapozhnik, H.-J. Elmers, M. Klaüi, and M. Jourdan, Nat. Commun. **9**, 348 (2018).
[17] M. Meinert, D. Graulich, and T. Matalla-Wagner, Phys. Rev. Applied **9**, 064040 (2018).
[18] S. Y. Bodnar, M. Filianina, S. P. Bommanaboyena, T. Forrest, F. Maccherozzi, A. A. Sapozhnik, Y. Skourski, M. Kläui, and M. Jourdan, Phys. Rev. B **99**, 140409(R) (2019).
[19] V. Saidl, P. Němec, P. Wadley, V. Hills, R. P. Campion, V. Novák, K. W. Edmonds, F. Maccherozzi, S. S. Dhesi, B. L. Gallagher, F. Trojánek, J. Kuneš, J. Železný, P. Malý, and T. Jungwirth, Nat. Photonics **11**, 91 (2017).
[20] Z. Sun, Y. Yi, T. Song, G. Clark, B. Huang, Y. Shan, S. Wu, D. Huang, C. Gao, Z. Chen, M. McGuire, T. Cao, D. Xiao, W.-T. Liu, W. Yao, X. Xu, and S. Wu, Nature (London) **572**, 497 (2019).
[21] J. Železný, P. Wadley, K. Olejník, A. Hoffmann, and H. Ohno, Nat. Phys. **14**, 220 (2018).
[22] D.-F. Shao, S.-H. Zhang, G. Gurung, W. Yang, and E. Y. Tsymbal, Phys. Rev. Lett. **124**, 067203 (2020).
[23] Y. Gao, S. A. Yang, and Q. Niu, Phys. Rev. B **91**, 214405 (2015).
[24] Y. Gao, Front. Phys. **14**, 33404 (2019).
[25] C. Xiao, H. Liu, J. Zhao, S. A. Yang, and Q. Niu, Phys. Rev. B **103**, 045401 (2021).
[26] C. Xiao, Y. Ren, and B. Xiong, Phys. Rev. B **103**, 115432 (2021).
[27] H. Liu, J. Zhao, Y. Huang, X. Feng, C. Xiao, W. Wu, S. Lai, W.-b. Gao, and S. A. Yang, arXiv:2106.04931.
[28] For degenerate bands and the summed m is out of the degenerate subspace.
[29] See Supplemental Material at http://link.aps.org/supplemental/10.1103/PhysRevLett.127.277202 for (i) detailed derivations of the Eq. (5), (ii) results for a 2D two-band Dirac model and PT symmetric Dirac models, (iii) DFT computation details, (iv) BCP dipole distribution versus Néel vector orientation, and (v) angular dependence of

second-order anomalous Hall conductivity of Mn_2Au, which includes Refs. [30–38].
[30] X. Xiao, S. A. Yang, Z. Liu, H. Li, and G. Zhou, Sci. Rep. **5**, 7898 (2015).
[31] S. Li, Y. Liu, Z.-M. Yu, Y. Jiao, S. Guan, X.-L. Sheng, Y. Yao, and S. A. Yang, Phys. Rev. B **100**, 205102 (2019).
[32] G. Kresse and J. Furthmüller, Phys. Rev. B **54**, 11169 (1996).
[33] G. Kresse and J. Furthmüller, Comput. Mater. Sci. **6**, 15 (1996).
[34] J. P. Perdew, K. Burke, and M. Ernzerhof, Phys. Rev. Lett. **77**, 3865 (1996).
[35] P. E. Blöchl, Phys. Rev. B **50**, 17953 (1994).
[36] G. Kresse and D. Joubert, Phys. Rev. B **59**, 1758 (1999).
[37] V. Barthem, C. Colin, H. Mayaffre, M.-H. Julien, and D. Givord, Nat. Commun. **4**, 2892 (2013).
[38] G. Pizzi *et al.*, J. Phys. Condens. Matter **32**, 165902 (2020).
[39] P. Tang, Q. Zhou, G. Xu, and S.-C. Zhang, Nat. Phys. **12**, 1100 (2016).
[40] L. Šmejkal, J. Železný, J. Sinova, and T. Jungwirth, Phys. Rev. Lett. **118**, 106402 (2017).
[41] D.-F. Shao, G. Gurung, S.-H. Zhang, and E. Y. Tsymbal, Phys. Rev. Lett. **122**, 077203 (2019).
[42] H.-C. Wu, Z.-M. Liao, R. G. S. Sofin, G. Feng, X.-M. Ma, A. B. Shick, O. N. Mryasov, and I. V. Shvets, Adv. Mater. **24**, 6374 (2012).
[43] V. Barthem, C. V. Colin, H. Mayaffre, M.-H. Julien, and D. Givord, Nat. Commun. **4**, 2892 (2013).
[44] M. Jourdan, H. Bräuning, A. Sapozhnik, H.-J. Elmers, H. Zabel, and M. Kläui, J. Phys. D **48**, 385001 (2015).
[45] K. Kang, T. Li, E. Sohn, J. Shan, and K. F. Mak, Nat. Mater. **18**, 324 (2019).
[46] S. Lai, H. Liu, Z. Zhang, J. Zhao, X. Feng, N. Wang, C. Tang, Y. Liu, K. S. Novoselov, S. A. Yang, and W.-b. Gao, Nat. Nanotechnol. **16**, 869 (2021).
[47] H. Watanabe and Y. Yanase, Phys. Rev. Research **2**, 043081 (2020).
[48] Q. Ma, S.-Y. Xu, H. Shen, D. MacNeill, V. Fatemi, T.-R. Chang, A. M. Mier Valdivia, S. Wu, Z. Du, C.-H. Hsu, S. Fang, Q. D. Gibson, K. Watanabe, T. Taniguchi, R. J. Cava, E. Kaxiras, H.-Z. Lu, H. Lin, L. Fu, N. Gedik, and P. Jarillo-Herrero, Nature (London) **565**, 337 (2019).
[49] C. Wang, Y. Gao, and D. Xiao, preceding Letter, Phys. Rev. Lett. **127**, 277201 (2021).